

## REVIEW

# Defect characterization in graphene and carbon nanotubes using Raman spectroscopy

BY M. S. DRESSELHAUS<sup>1,\*</sup>, A. JORIO<sup>2,\*</sup>, A. G. SOUZA FILHO<sup>3,\*</sup>  
AND R. SAITO<sup>4,\*</sup>

<sup>1</sup>*Department of Physics and Department of Electrical Engineering and  
Computer Science, Massachusetts Institute of Technology, Cambridge,  
MA 02139-4307, USA*

<sup>2</sup>*Departamento de Física, Universidade Federal de Minas Gerais,  
Belo Horizonte - MG, 30123-970, Brazil*

<sup>3</sup>*Departamento de Física, Universidade Federal do Ceará,  
Fortaleza - CE, 60455-900, Brazil*

<sup>4</sup>*Department of Physics, Tohoku University, Sendai 980-8578, Japan*

This review discusses advances that have been made in the study of defect-induced double-resonance processes in nanographite, graphene and carbon nanotubes, mostly coming from combining Raman spectroscopic experiments with microscopy studies and from the development of new theoretical models. The disorder-induced peak frequencies and intensities are discussed, with particular emphasis given to how the disorder-induced features evolve with increasing amounts of disorder. We address here two systems, ion-bombarded graphene and nanographite, where disorder is represented by point defects and boundaries, respectively. Raman spectroscopy is used to study the ‘atomic structure’ of the defect, making it possible, for example, to distinguish between zigzag and armchair edges, based on selection rules of phonon scattering. Finally, a different concept is discussed, involving the effect that defects have on the lineshape of Raman-allowed peaks, owing to local electron and phonon energy renormalization. Such effects can be observed by near-field optical measurements on the  $G'$  feature for doped single-walled carbon nanotubes.

**Keywords:** graphene; nanographite; carbon nanotubes; Raman spectroscopy; defects

## 1. Introduction: an historical overview

In general, disorder-induced symmetry-breaking effects play a very important role in the determination of several material properties, such as transport properties and the relaxation of photo-excited carriers. In particular,  $sp^2$  carbons, which have

\*Authors for correspondence (millie@mgm.mit.edu, adojorio@fisica.ufmg.br, agsf@fisica.ufc.br, rsaito@flex.phys.tohoku.ac.jp).

One contribution of 12 to a Theme Issue ‘Electronic and photonic properties of graphene layers and carbon nanoribbons’.

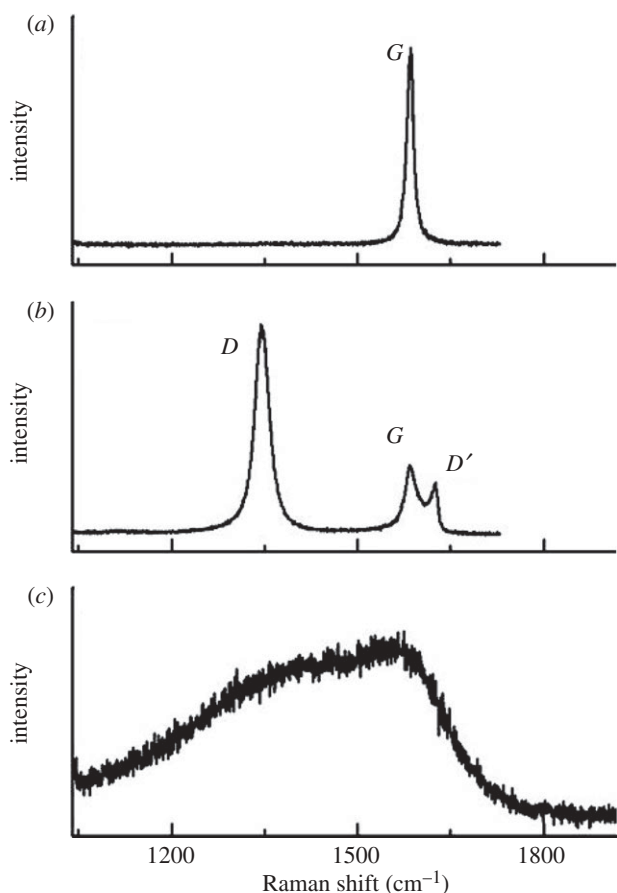


Figure 1. The first-order Raman spectrum of (a) crystalline graphene, (b) defective graphene and (c) highly disordered single-layer graphene deposited on a SiO<sub>2</sub> substrate. These spectra are all obtained with  $E_{\text{laser}} = 2.41$  eV (Jorio *et al.* 2010a).

high symmetry, are highly sensitive to symmetry-breaking defects. Disorder and symmetry breaking are observed sensitively by spectroscopy, which depends strongly on crystal symmetry (Ashcroft & Merman 1976; Kittel 1986). The presence of disorder in  $sp^2$  hybridized carbon systems leads to rich and intriguing phenomena in their resonance Raman spectra, thus making Raman spectroscopy one of the most sensitive and informative techniques to characterize disorder in  $sp^2$  carbon materials. Raman spectroscopy has thus become a key tool and is widely used to identify disorder in the  $sp^2$  network of different carbon structures, such as diamond-like carbon (DLC), amorphous carbon, nanostructured carbon, as well as carbon nanofibres, nanotubes and nanohorns and most recently graphene (Ferrari & Robertson 2004; Novoselov *et al.* 2005; Zhang *et al.* 2005; Pimenta *et al.* 2007; Jorio *et al.* 2008).

The Raman spectrum of crystalline graphite is marked by the presence of two strong peaks centred at 1580 and 2700 cm<sup>-1</sup>, named the  $G$  and  $G'$  bands, respectively, where the  $G$  label refers to graphite (figure 1). The

$G$  band is a first-order Raman-allowed feature originating from the zone centre (phonon-wavevector  $q = 0$ ), corresponding to the in-plane optical phonon modes (Tuinstra & Koenig 1970*a,b*). The  $G'$  band is a second-order (two phonon) feature that allows exploration of  $q \neq 0$  phonons (Nemanich & Solin 1977, 1979).

In the Raman spectra obtained from samples with small crystallite size  $L_a$  (less than  $0.5\ \mu\text{m}$ , i.e. smaller than the wavelength of light), the presence of an additional dispersive peak centred at approximately  $1350\text{ cm}^{-1}$  is observed when using laser excitation at  $2.41\text{ eV}$ . This feature is assigned to the breathing of the carbon hexagons that become Raman active at the borders of the crystallite areas owing to the loss of translational symmetry (Tuinstra & Koenig 1970*a,b*). The frequency of this feature is about half of the second-order  $G'$  frequency, and is related to the phonon of the first-order process of the  $G'$  peak. Since the approximately  $1350\text{ cm}^{-1}$  peak is observed in the presence of defects in an otherwise perfect infinite graphite structure, it has been named the  $D$  band ( $D$  for defect or disorder). Therefore, its intensity is proportional to the amount of disorder (crystallite boundary) in the sample, and the ratio between the intensities of the disorder-induced  $D$  band and the first-order graphite  $G$  band ( $I_D/I_G$ ) provides a parameter that can be used for quantifying disorder.

In 1970, it was shown that the  $D$  to  $G$  band intensity ratio (Tuinstra & Koenig 1970*a,b*) is correlated with crystallite size  $L_a$  by the relation  $I_D/I_G = A/L_a$ , where  $A$  is a constant for a fixed laser excitation energy. This relation can be applied to large enough carbon  $sp^2$  crystallites (Knight & White 1989), while the complete amorphization trajectory for  $I_D/I_G$  going down to small  $L_a$  values was proposed. The  $I_D/I_G$  ratio starts to decrease for very small values of  $L_a$  (a few nanometers) because the  $sp^2$  carbon hexagonal structure then starts to disappear. Furthermore, this  $I_D/I_G$  intensity ratio was shown to be excitation laser energy dependent (Mernagh *et al.* 1984). Another disorder-induced band centred at  $1620\text{ cm}^{-1}$  is usually observed in the Raman spectra of disordered graphitic materials, although with smaller intensity than the  $D$  band. This feature, reported by Tsu *et al.* (1978), has been named the  $D'$  band and also depends on  $L_a$  and  $E_{\text{laser}}$ .

In 1981, it was shown (Vidano *et al.* 1981) that the  $D$  and  $G'$  bands are dispersive, i.e. their frequencies change with the incident laser energy  $E_{\text{laser}}$ , with  $\Delta\omega_D/\Delta E_{\text{laser}} \sim 53\text{ cm}^{-1}\text{ eV}^{-1}$  and  $\Delta\omega_{G'}/\Delta E_{\text{laser}} \sim 106\text{ cm}^{-1}\text{ eV}^{-1}$ . The out-of-plane stacking order has also been shown to affect the  $G'$  Raman lineshape (Lespade *et al.* 1982, 1984; Wilhelm *et al.* 1998). Baranov *et al.* (1987) proposed that the dispersive behaviour of the  $D$  band comes from the coupled resonance between the excited electrons and the scattered phonons, as previously discussed in semiconductor physics (Martin & Falicov 1975; Cardona 1982). The full appreciation of the double-resonance model came in 2000, as discussed by Thomsen & Reich (2000), and their model was extended by Saito *et al.* (2002) to explain the mechanism behind many other dispersive Raman peaks usually observed in the literature, yielding an explanation for all the features observed in the Raman spectra of ordered and disordered graphite (Ferrari & Robertson 2000). Many of the weak Raman features are dispersive and can be used to determine the graphite phonon dispersion (Saito *et al.* 2002). In fact, the atomic vibrations with different wavevectors are usually observed by inelastic neutron scattering, making use of momentum conservation requirements. Another

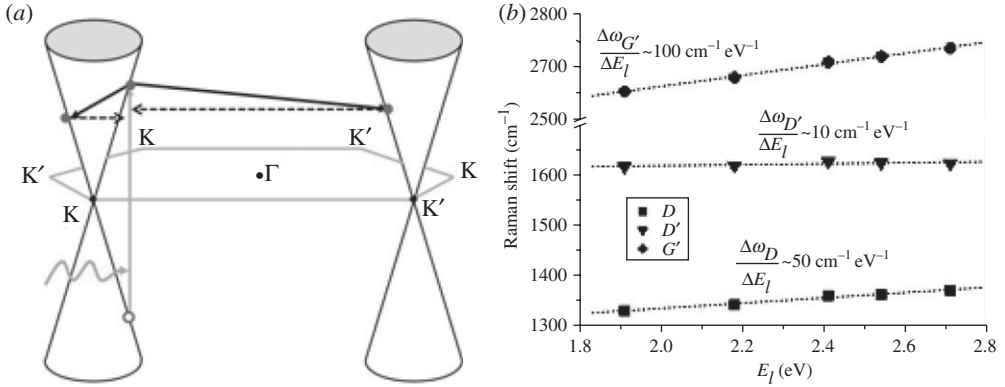


Figure 2. (a) Schematic showing the electronic dispersion near the Fermi level at the K and K' points in the hexagonal Brillouin zone of graphene. The light-induced electron-hole formation is indicated by a grey arrow. The two resonant electron-phonon scattering processes associated with the *D* (inter-valley) band and the *D'* (intra-valley) band are indicated by the black arrows. The dashed arrows indicate elastic scattering induced by defects. (b) Laser energy dependence or dispersion of the frequency of the *D*, *D'* and *G'* bands (Pimenta *et al.* 2007).

interesting result obtained by the double-resonance model (discussed below) was the identification of the atomic structure at graphite and graphene ribbon edges (Cançado *et al.* 2004).

## 2. Double-resonance Raman scattering

Defects break the momentum conservation requirement for first order  $q=0$  Raman-allowed phonons, so that, in principle, any scattering event involving phonons in the interior of the Brillouin zone ( $q \neq 0$ ) would then be allowed. However, in  $sp^2$  carbon materials the resonant electron-phonon scattering processes connecting real electronic states (figure 2a) minimize the denominators in the resonance Raman intensity (or cross section) which are given by (Dresselhaus *et al.* 2005)

$$I(\omega, E_{\text{laser}}) = \sum_i \left| \sum_{a,b,c,\omega_{\text{ph}}} \frac{M_{\text{op}}(k, ic) M_{\text{d}}(-q, cb) M_{\text{ep}}(q, ba) M_{\text{op}}(k, ai)}{\Delta E_{ai}(\Delta E_{bi} - \hbar\omega_{\text{ph}})(\Delta E_{ai} - \hbar\omega_{\text{ph}})} \right|^2, \quad (2.1)$$

where  $\Delta E_{ai} = (E_{\text{laser}} - (E_a - E_i) - i\gamma_r)$  and  $\gamma_r$  denotes a broadening factor. Here subscripts  $i, a, b$  and  $c$ , respectively, denote the initial state, the excited state, the first scattered state of an electron by a phonon and the second scattered state of an electron by a defect.  $M_{\text{op}}$ ,  $M_{\text{ep}}$  and  $M_{\text{d}}$  denote the electron-photon, electron-phonon and electron-defect scattering matrix elements, respectively, and we use the fact that  $E_b = E_c$  since the scattering from  $b$  to  $c$  is an elastic scattering process. These resonant processes enhance the scattering amplitude much more than for non-resonant processes, so that the spectra are dominated by the double-resonance *D* and *D'* band scattering processes, fulfilling energy and momentum conservation. While momentum conservation in a perfect lattice can only be

fulfilled by two-phonon scattering processes ( $G'$  band), momentum conservation in the presence of disorder can be satisfied through an elastic scattering process by a defect, represented by dashed arrows in figure 2a.

The dispersion of the frequency of the  $D$ ,  $D'$  and  $G'$  bands is shown in figure 2b by plotting their frequency dependence on  $E_{\text{laser}}$ , and these features are well explained by the double-resonance model. The slope associated with the  $G'$  band is about  $106 \text{ cm}^{-1} \text{ eV}^{-1}$  and, as stated above, is two times larger than the slope of the  $D$  band ( $53 \text{ cm}^{-1} \text{ eV}^{-1}$ ). The  $D'$  band also exhibits a weak dispersive behaviour, the slope being approximately  $10 \text{ cm}^{-1} \text{ eV}^{-1}$  (Pimenta *et al.* 2007).

The  $D$  and  $D'$  bands are not the only disorder-induced one-phonon peaks in the Raman spectra for disordered  $sp^2$  materials. Any combination or overtone of the six dispersive phonon energy branches in graphene can occur and disorder-induced Raman frequencies can be related to any of the six phonon branches of two-dimensional graphite with the appropriate wavevector which fulfils the double-resonance condition. The intra-valley and inter-valley double-resonance processes are mediated by phonons near the  $\Gamma$  and K (or K') points, respectively, and we can vary both the resonant  $k$  and  $q$  values by changing  $E_{\text{laser}}$ , as determined by conservation of energy and momentum requirements. Thus by using electronic band structure information, we can determine the phonon dispersion relations around the K and the  $\Gamma$  points, by considering inter-valley and intra-valley processes, respectively. This approach has been used for obtaining the graphene phonon dispersion relations using Raman spectroscopy, as reported by Saito *et al.* (2002).

### 3. Quantifying disorder in graphene and nanographite from Raman intensity analysis

The frequencies of the disorder-induced features in the Raman spectra for  $sp^2$  carbons are well explained by the double-resonance model. What remains to be established for making Raman spectroscopy an even more powerful tool to characterize disorder in  $sp^2$  materials is how to relate specific defects to their corresponding disordering processes, and how to obtain quantitative information about the amount of each type of lattice defect.

To achieve a quantitative description of these phenomena, the effects of disorder on the electron and phonon properties have to be probed in both momentum space ( $k$ -space) and real space ( $r$ -space), which means Raman spectroscopy has to be combined with microscopy experiments. Transmission electron microscopy (TEM) or scanning tunnelling microscopy (STM) can characterize disorder of the crystal in  $r$ -space by probing the local surface density of electronic states, with atomic-level resolution. Simultaneous *in situ* TEM and Raman measurements are possible (Meyer *et al.* 2005). However, a special experimental set-up and special sample preparation methods would be needed. Usually, STM and Raman spectroscopy cannot be easily correlated with each other, since optical spectroscopy probes a volume that is limited by the light penetration depth, while STM is mostly sensitive to surfaces. In this context, the possibility of exfoliating graphite to pull out a single graphene sheet provides an ideal situation in which microscopy and spectroscopy can be correlated to probe disorder effects in both  $r$ -space and  $k$ -space for the same sample. The initial efforts in this research direction are now discussed.

*(a) Point defects induced by ion bombardment*

The controlled use of ion implantation to study defects in  $sp^2$  carbons is a well-established technique (Dresselhaus & Kalish 1992). These experiments are normally carried out as a function of ion dose and for different ion species and different ion energies. Low-mass ions at low ion fluence introduce point defects. Increasing the ion dose causes an increasing density of point defects and eventually causes the damaged regions to overlap, as discussed for ion-bombarded highly ordered pyrolytic graphite (HOPG) (Jorio *et al.* 2009) and graphene (Jorio *et al.* 2010*a,b*, in press; Lucchese *et al.* 2010; Ferreira *et al.* in press).

Consecutive  $\text{Ar}^+$  ion bombardment and Raman spectroscopy experiments were performed on monolayer graphene samples (Lucchese *et al.* 2010) using low-energy ions to avoid cascade effects. Cascade effects are effects whereby a scattered C atom with a large energy hits another C atom iteratively, similar to the chain reaction of dominoes. The bombarding ion doses vary from  $10^{11}$  to  $10^{15} \text{Ar}^+ \text{cm}^{-2}$ , which correspond, respectively, to one defect per  $4 \times 10^4$  C atoms and to the onset of full disorder in graphene. The defect density in real space was monitored by STM images, which allowed the extraction of the defect density or alternatively values of the average distances between defects (Lucchese *et al.* 2010). For the highest ion doses of  $10^{15} \text{Ar}^+ \text{cm}^{-2}$ , where the defect-induced regions start to coalesce, we consider that the defect density increases linearly with bombardment time.

Figure 3 shows the Raman spectra of a graphene monolayer subjected to different ion bombardment intensities. From the pristine sample (bottom spectrum) to the lowest bombardment dose in figure 3*a* ( $10^{11} \text{Ar}^+ \text{cm}^{-2}$ ), the  $D$ -band process is activated, showing a very small intensity relative to the  $G$  peak. Within the bombardment dose range  $10^{11}$ – $10^{13} \text{Ar}^+ \text{cm}^{-2}$ , the intensities of the disorder-induced peaks increase. The second disorder-induced peak around approximately  $1620 \text{cm}^{-1}$  (the  $D'$  band) also becomes evident. Above  $10^{13} \text{Ar}^+ \text{cm}^{-2}$ , the Raman spectra start to broaden significantly and end up exhibiting a profile similar to the graphene phonon density of states (PDOS) for the highest ion dose (Lucchese *et al.* 2010).

By plotting the  $I_D/I_G$  data as a function of the average distance between defects  $L_D$ , as shown in figure 3*b*, it is possible to quantify the disorder evolution in the graphene layer. The  $I_D/I_G$  ratio has a non-monotonic dependence on  $L_D$ , increasing initially with increasing  $L_D$  up to  $L_D \sim 3.5 \text{nm}$ , where  $I_D/I_G$  in figure 3*b* has a peak value, and then decreasing for  $L_D > 3.5 \text{nm}$ . This result is similar to the proposed amorphization trajectory for graphitic nanocrystallites, and such a behaviour suggests the existence of two disorder-induced competing mechanisms contributing to the Raman  $D$ -band intensity, which we describe next.

*(b) Model for the D-band activated region*

The results of figure 3 are modelled in figure 4 by assuming that a single impact of an ion on the graphene sheet causes modifications on two length scales, here denoted by  $r_A$  and  $r_S$  (with  $r_A > r_S$ ), which are the radii of two circular areas measured from the ion impact point (see figure 4). Within the shorter radius  $r_S$ , a structurally disordered  $S$ -region occurs relative to the point of impact. For distances larger than  $r_S$  but shorter than  $r_A$ , the lattice structure is preserved,



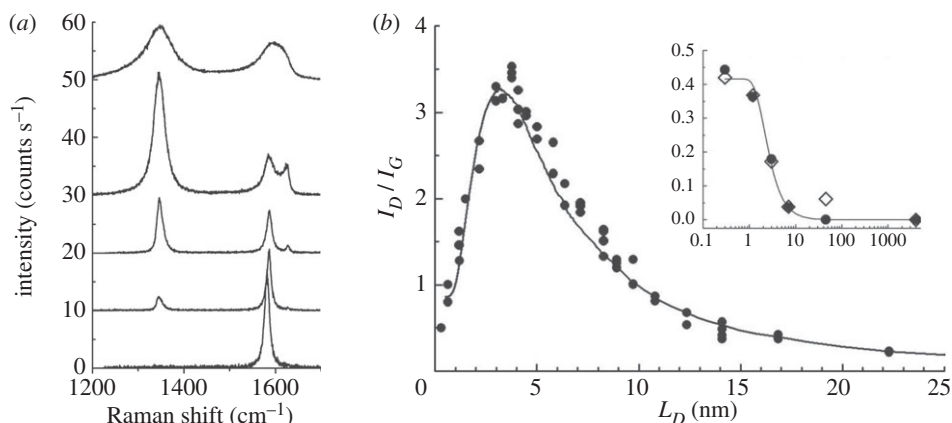


Figure 3. (a) Evolution of the first-order Raman spectra (using a  $\lambda = 514$  nm laser) taken from a graphene monolayer sample deposited on an SiO<sub>2</sub> substrate, subjected to Ar<sup>+</sup> ion bombardment. The ion doses are from the bottom to the top,  $10^{10}$ ,  $10^{11}$ ,  $10^{12}$ ,  $10^{13}$  and  $10^{14}$  Ar<sup>+</sup> cm<sup>-2</sup> (Lucchese *et al.* 2010). (b) The  $I_D/I_G$  data points from three different monolayer graphene samples as a function of the average distance  $L_D$  between defects. The solid line is a modelling of the experimental data with equation (3.1). The inset shows a plot of  $I_D/I_G$  versus  $L_D$  on a log scale for  $L_D$  for two samples: (i) open points for an approximately 50-layer graphene sample and solid circles are for a small piece of HOPG near a graphene piece and (ii) solid diamond points, for a 2 mm thick bulk HOPG sample, the measured values of which are here scaled by  $(I_D/I_G) \times 3.5$  (Lucchese *et al.* 2010).

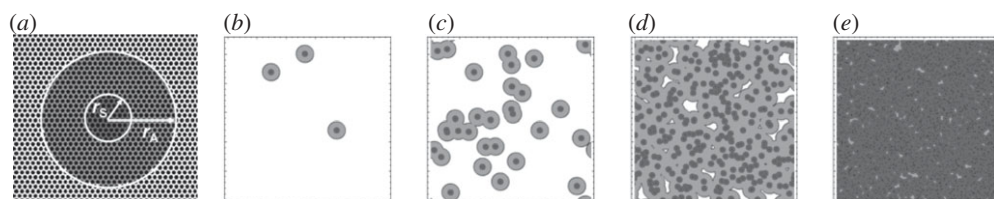


Figure 4. (a) Definition of the ‘activated’ A-region (darkest grey) and ‘structurally disordered’ S-region (dark grey). The radii are measured from the ion impact point, which is chosen randomly in our simulation. (b–e) shows 55 × 55 nm portions of the graphene simulation cell, with snapshots of the structural evolution of the graphene sheet for different defect concentrations. (b)  $10^{11}$  Ar<sup>+</sup> cm<sup>-2</sup>, (c)  $10^{12}$  Ar<sup>+</sup> cm<sup>-2</sup>, (d)  $10^{13}$  Ar<sup>+</sup> cm<sup>-2</sup> and (e)  $10^{14}$  Ar<sup>+</sup> cm<sup>-2</sup>, as in figure 3 (Lucchese *et al.* 2010).

but the proximity between defects causes a mixing of Bloch states near the K and K' valleys of the graphene Brillouin zone, thus causing a breakdown of the selection rules, and leading to an enhancement of the D-band intensity. We call this the activated or A-region. In qualitative terms, an electron–hole excitation will only be able to ‘see’ the structural defect if the electron–hole pair is created sufficiently close to the defect site and if the excited electron (or hole) lives long enough for the defective region to be probed by Raman spectroscopy. If the Raman scattering process occurs at distances larger than  $\ell = r_A - r_S$  from the ion impact point, the wavevector  $k$  is a good quantum number for analysing

the scattering selection rules and those regions that remain well ordered will only contribute significantly to the  $G$ -band feature in the Raman spectra, and not to symmetry-breaking features. Our phenomenological model for the  $I_D/I_G$  ratio is given as a function of the average distance between two defects,  $L_D$ ,

$$\frac{I_D}{I_G}(L_D) \propto I_D(L_D) = C_A f_A(L_D) + C_S f_S(L_D), \quad (3.1)$$

where  $I_G$  is considered to be a constant (independent of  $L_D$ ), and  $f_A$  and  $f_S$  are simply the fractions of the  $A$  and  $S$  areas, respectively, with respect to the total area in the graphene sheet. Although both the  $A$  and  $S$  regions can break momentum conservation, giving rise to a  $D$  band, the  $A$  regions will contribute most strongly to the  $D$  band, while the  $S$  regions will make less contribution to the  $D$  band owing to the breakdown of the lattice structure itself.

Stochastic simulations were performed for implementing the phenomenological model and they are discussed in detail in Lucchese *et al.* (2010). Snapshots of the disorder evolution are shown in figure 4*b–e* for the same argon ion concentrations as in figure 3*a*. The stochastic simulations of the bombardment process, with the impact points for the ions chosen at random, combined with equation (3.1) and using the parameters  $C_A = 4.56$ ,  $C_S = 0.86$ ,  $r_A = 3$  nm and  $r_S = 1$  nm, give the full line curve in figure 3*b*, which is in excellent agreement with the experimental results (points) in this figure (Lucchese *et al.* 2010).

The non-monotonic behaviour in figure 3*b* can be understood by considering that, for low defect concentrations (large  $L_D$ ), the total area contributing to  $D$ -band scattering is proportional to the number of defects, thus giving rise to a  $I_D/I_G = (102 \pm 2)/L_D^2$  dependence that works well for  $L_D > 2r_A$ . Upon increasing the defect concentration, the activated regions start to overlap and these regions eventually saturate. The  $D$ -band intensity then reaches a maximum and a further increase in the defect concentration decreases the  $D$ -band intensity because the graphene sheet starts to be dominated by the structurally disordered areas.

The length scale  $r_S = 1$  nm, which defines the structurally disordered area, is in excellent agreement with the average size of the disordered structures seen in the STM images. This parameter should, however, not be universal, but it should be specific to the bombardment process and ion bombardment conditions. The Raman relaxation length  $\ell$  for the defect-induced resonant Raman scattering in graphene for  $E_{\text{laser}} = 2.41$  eV (514 nm) is found to be  $\ell = r_A - r_S = 2$  nm. Here, we discuss the relaxation length for the excited electron, and this should not be confused with the relaxation length for the phonons. The  $C_A$  parameter in equation (3.1) is a measure of the maximum possible value of the  $I_D/I_G$  ratio in graphene, which would occur in a hypothetical situation in which K–K' wavevector mixing would be allowed everywhere, but no damage would be made to the hexagonal network of carbon atoms.  $C_A$  should then be defined by the electron–phonon matrix elements, and the value  $C_A = 4.56$  is then in rough agreement with the ratio between the electron–phonon coupling for the iTO phonons evaluated between the  $\Gamma$  and K points in the Brillouin zone (Lazzeri *et al.* 2008). The  $C_S$  parameter is then the value of the  $I_D/I_G$  ratio in the highly disordered limit, which has not yet been addressed theoretically.



Finally, for practical use, it is important to have an equation relating  $I_D/I_G$  to  $L_D$ , and such an equation can be obtained by solving the rate equations for the bombardment process. The entire regime ( $0 \rightarrow L_D \rightarrow \infty$ ) can be fitted using

$$\frac{I_D}{I_G} = C_A \frac{r_A^2 - r_S^2}{r_A^2 - 2r_S^2} \left[ \exp\left(\frac{-\pi r_S^2}{L_D^2}\right) - \exp\left(\frac{-\pi(r_A^2 - r_S^2)}{L_D^2}\right) \right] + C_S \left[ 1 - \left(\frac{-\pi r_S^2}{L_D^2}\right) \right]. \quad (3.2)$$

Fitting the data in [figure 3b](#) with equation (3.2) gives  $C_A = (4.2 \pm 0.1)$ ,  $C_S = (0.87 \pm 0.05)$ ,  $r_A = (3.00 \pm 0.03)$  nm and  $r_S = (1.00 \pm 0.04)$  nm, also in excellent agreement with experiment and consistent with the parameters obtained by computational modelling ([Lucchese \*et al.\* 2010](#)).

The model of equation (3.2) provides a method to accurately quantify the density of defects  $\sigma$  or, equivalently, the average distance between defects ( $L_D = \sigma^{-1/2}$ ) in graphene. As the defects start to coalesce, the expected behaviour occurs, and here  $I_D/I_G = A/L_D^2$ , where  $A = (102 \pm 2)$  nm<sup>2</sup> and  $L_D > 6$  nm. When the defects start to coalesce, there is a competition between the two disorder mechanisms, and equation (3.2) can be used to determine the relative importance of each mechanism quantitatively. The present results discussed for graphene are similar to what has been observed in ion-bombarded graphite (HOPG) ([Jorio \*et al.\* 2009](#)), although some details are different. First, for HOPG a more intense *G* band is always observed owing to the contribution from the undisturbed under-layers. Second, for graphene, above  $10^{15}$  Ar<sup>+</sup> cm<sup>-2</sup>, the Raman spectra show a decreased intensity, indicating full amorphization or partial sputtering of the graphene layer. For HOPG, above  $10^{15}$  Ar<sup>+</sup> cm<sup>-2</sup>,  $I_D/I_G$  saturates and no further change is observed in the Raman spectra because of the large number of layers that have been amorphitized and/or sputtered. This behaviour is seen in the inset to [figure 3b](#), which shows the  $I_D/I_G$  evolution for two HOPG samples of different thicknesses. Despite differences in absolute values, which depend on the number of undisturbed under-layers (the data given by the diamond-shaped points in the inset to [figure 3b](#) coming from a thicker HOPG sample were scaled by  $\times 3.5$ ), the  $I_D/I_G$  values increase and saturate at about  $L_D = 9$  nm when increasing the ion dose.

### (c) One-dimensional defects represented by the boundaries of nanocrystallites

Next let us discuss the *D*-band image at the edges of nanographite. The defect associated with an edge has a one-dimensional character and it is only able to transfer momentum in the direction perpendicular to the edge. [Figure 5a,b](#) shows two confocal Raman images of a 6 nm high HOPG crystallite deposited on a glass substrate. [Figure 5a](#) shows a Raman image of the crystallite, obtained by plotting a spatial dependence map of the *G*-band intensity, while in [figure 5b](#) a similar spatial dependence of the intensity of the disorder-induced *D* band is shown and here the boundary of the crystallite is highlighted. [Figure 5c](#) shows two Raman spectra, one taken at an interior point of the crystallite and the other at the edge. It is clear from [figure 5a–c](#) that the *G*-band intensity is uniform over the whole graphite surface, while the *D*-band intensity is localized where the crystalline structure is not perfect, mostly at the edges of the crystallite. The

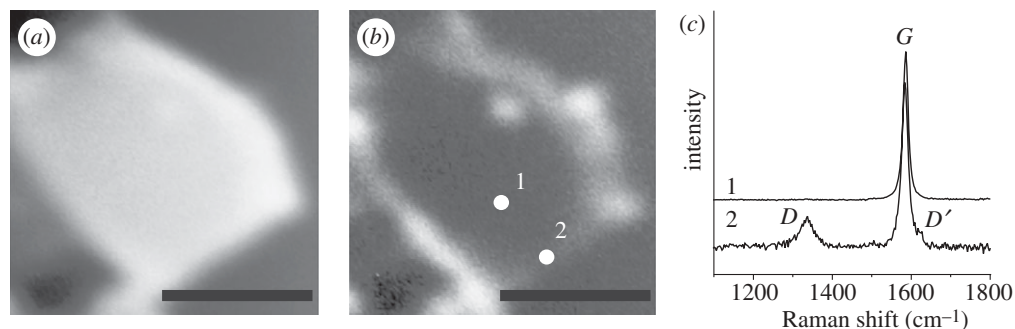


Figure 5. (a) *G*-band and (b) *D*-band confocal (300 nm resolution) Raman images of a graphite crystallite deposited on a glass substrate. In (c) the Raman spectra obtained in regions 1 and 2 (white circles depicted in (b)) are shown. The laser excitation comes from a HeNe ( $\lambda = 633$  nm (1.92 eV)) laser using an experimental set-up described in Pimenta *et al.* (2007). Scale bars, (a,b) 2  $\mu$ m.

edge also behaves like a symmetry-breaking effect and causes *D*-band intensity. Note also that the *D*-band intensity varies from edge to edge, and this *D*-band intensity is dependent on the light polarization direction and the atomic structure at the edge, as discussed in this section.

For evaluation of the  $I_D/I_G$  dependence on the crystallite dimensions, one can consider a square of side  $L_a$ , for which the intensity of the *G* band will vary as  $I_G \propto L_a^2$ , where  $L_a$  is the mean crystallite size. The intensity of the *D* band will, however, depend on the width  $\delta$  of the ‘border’ where the *D* band is activated, and is given by  $I_D \propto L_a^2 - (L_a - 2\delta)^2$ . The intensity ratio will then be given by

$$\frac{I_D}{I_G} = \alpha \left[ 4 \left( \frac{\delta}{L_a} - \frac{\delta^2}{L_a^2} \right) \right], \quad (3.3)$$

where  $\alpha$  is dependent on the appropriate matrix elements (Pimenta *et al.* 2007).

In the limit  $L_a \gg \delta$ , equation (3.3) can be simplified to yield the Tuinstra–Koenig relation

$$\frac{I_D}{I_G} = \frac{C(E_{\text{laser}})}{L_a}, \quad (3.4)$$

where the value of the empirical constant  $C(E_{\text{laser}})$  depends on  $E_{\text{laser}}$ . One could then expect that, once the relaxation length and matrix element ratio were measured for the *D*-band scattering in ion-bombarded graphene, these values could just be used to obtain  $\alpha$  and  $\delta$ . However, the relaxation length and matrix element ratio depend on the structurally disordered area ( $S_S$ ), which is not well defined for nanographite. Figure 6 shows two STM images with atomic resolution obtained from the surface of a crystallite in a nanographite sample with  $L_a = 65$  nm. The atomic arrangement of the carbon atoms observed in these images indicates that the samples are formed by nanographitic crystallites, with a disordered grain boundary between crystallites (Cançado *et al.* 2007). Variability associated with grain boundaries such as in figure 6 may also be responsible for the different  $I_D/I_G$  versus  $L_a$  results observed in the literature.

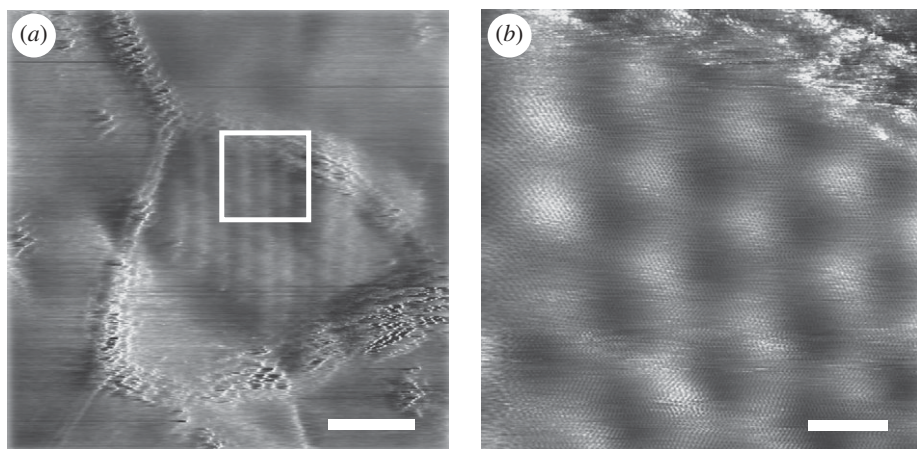


Figure 6. Scanning tunnelling microscopy (STM) images with atomic resolution obtained from the surface of a nanographite crystallite of a sample with  $L_a = 65$  nm. (a) A moiré pattern at the crystallite surface is observed (scale bar, 25 nm). (b) Magnification of the region delineated by the white square in (a), where the carbon atom positions in the graphite lattice can be more clearly observed (Cançado *et al.* 2007; scale bars (a,b), 5 nm).

Furthermore, the empirical constant  $C(E_{\text{laser}})$  has been known to depend on  $E_{\text{laser}}$  since 1984 (Mernagh *et al.* 1984), but  $C(E_{\text{laser}})$  has been quantitatively determined only more recently (Cançado *et al.* 2008), using experimental results from nanographites with different  $L_a$  values prepared from DLC films heat treated at different temperatures  $T_{\text{htt}}$  (Cançado *et al.* 2008). The  $L_a$  sizes were determined by using both STM and X-ray measurements and these  $L_a$  values were correlated with the  $I_D/I_G$  intensity ratios measured at different laser energies leading to a general equation for determining  $I_D/I_G$  independent of laser excitation energy (Cançado *et al.* 2008). This empirical equation was developed as follows. Shown in figure 7a are the results from Raman scattering experiments performed at room temperature with different  $E_{\text{laser}}$  values, showing spectra of the D, G and D' bands for the  $T_{\text{htt}} = 2000^\circ\text{C}$  sample ( $L_a = 35$  nm) for five different  $E_{\text{laser}}$  values. The spectra are normalized to the G band intensity, and clearly the ratio ( $I_D/I_G$ ) is strongly dependent on  $E_{\text{laser}}$ . Figure 7b shows the Raman spectra using  $E_{\text{laser}} = 1.92$  eV for samples with different  $T_{\text{htt}}$  values, thereby giving rise to samples with different crystallite sizes  $L_a$  (Cançado *et al.* 2008).

Figure 8a shows a plot of ( $I_D/I_G$ ) versus  $1/L_a$  for all samples shown in figure 7. Noting that  $I_D/I_G$  for a given sample is strongly dependent on  $E_{\text{laser}}$ , we see that all these curves collapse onto the same curve in the  $(I_D/I_G)E_{\text{laser}}^4$  versus  $L_a$  plot shown in figure 8b, demonstrating that a general equation is obtained for the determination of the nanographite crystallite size  $L_a$  using any laser line in the visible range (Cançado *et al.* 2008)

$$L_a(\text{nm}) = \frac{560}{E_{\text{laser}}^4} \left( \frac{I_D}{I_G} \right)^{-1} = (2.4 \times 10^{-10}) \lambda_{\text{laser}}^4 \left( \frac{I_D}{I_G} \right)^{-1}, \quad (3.5)$$

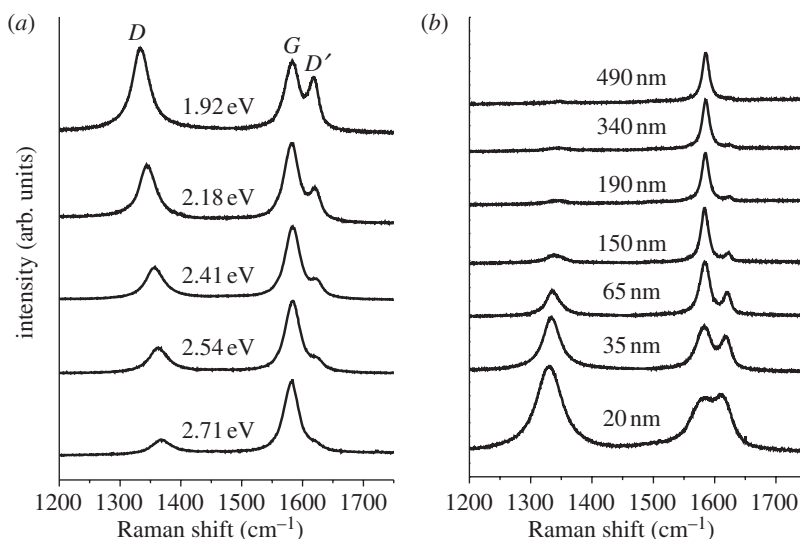


Figure 7. (a) The first-order Raman spectra of a nanographite sample heat treated at 2000°C ( $L_a = 35$  nm), for five different laser energy values (1.92, 2.18, 2.41, 2.54 and 2.71 eV). (b) Nanographite samples with different crystallite sizes  $L_a$  using 1.92 eV laser excitation energy (Cançado *et al.* 2008).

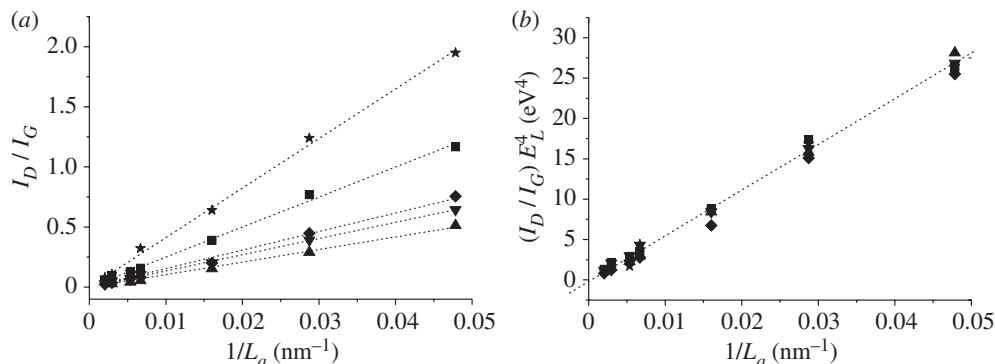


Figure 8. (a) The intensity ratio  $I_D/I_G$  for nanographite samples is plotted versus  $1/L_a$  using five different laser excitation energies (filled star, 1.92 eV; filled square, 2.18 eV; filled diamond, 2.41 eV; filled inverted triangle, 2.54 eV; filled triangle, 2.71 eV; see text). (b) All curves shown in (a) collapse onto the same curve in the  $(I_D/I_G)E_L^4$  versus  $(1/L_a)$  plot where  $E_L \equiv E_{\text{laser}}$  (Cançado *et al.* 2008).

where the laser excitation is given in terms of both  $E_{\text{laser}}$  (eV) and wavelength  $\lambda_{\text{laser}}$  (nm). The samples used for establishing the empirical equation (3.5) can be considered as model samples and the use of equation (3.5) for any general  $sp^2$  carbon-based material would probably need to be generalized. One example of such a study has been made for carbon foams (Barros *et al.* 2005).

## (d) Absolute Raman cross section

Measuring the absolute cross section for the Raman scattering processes is challenging, since the Raman signal depends strongly on the specific set-up (specific optics), on alignment and on  $E_{\text{laser}}$ . This is the reason why the intensity ratio  $I_D/I_G$  has been used systematically for quantifying disorder. Some argue that the intensity ratio  $I_D/I_{G'}$  should instead be chosen because both the  $D$  and  $G'$  bands involve a very similar phonon (inter-valley iTO,  $q \approx 2k$ ). However, the  $D$  and  $G'$  bands differ strongly in energy, and different Raman set-ups would give different responses for a given sample.

However, Cançado *et al.* (2007) have done all the calibration procedures for measuring the absolute Raman cross section of the  $D$ ,  $G$ ,  $D'$  and  $G'$  bands. In this work, the dependence of  $I_D/I_G$  on  $L_a$  was shown to come from  $I_D$ , while  $I_G$  was found to be independent of  $L_a$  within the measured  $L_a$  range (from 20 to 500 nm). For the  $E_{\text{laser}}$  dependence, the double-resonance features were shown to be  $E_{\text{laser}}$  independent, while  $I_G$  shows the  $E_{\text{laser}}^4$  dependence expected from scattering theory, as discussed above (Cançado *et al.* 2007). It is not yet known whether the  $E_{\text{laser}}^4$  dependence will also be observed for zero-dimensional (e.g. ion-induced) defective graphene. Actually, one of the open fields in the Raman spectroscopy of  $sp^2$  carbons is what rules determine the intensity of the double-resonance features. Some theoretical work has been done (Sato *et al.* 2006; Basko 2008) on this topic, but the results are still not at the level of explaining actual experimental observations.

#### 4. Defect-induced selection rules: dependence on the edge atomic structure

Besides defect quantification, it is important to discuss how disorder depends on the specific defect. An example of a result that was successful in distinguishing different defects from one another is the study of the edge of a graphite sample, analysing the orientation of the carbon hexagons with respect to the edge axis, thereby distinguishing the so-called zigzag edge arrangements from the armchair or random atomic edge structures (Cançado *et al.* 2004). As discussed here, the armchair (zigzag) structure can be identified spectroscopically by the presence (absence) of the  $D$  band. This effect can be understood by applying double-resonance theory to a semi-infinite graphite crystal and by considering the one-dimensional character of the defect, as discussed below.

Figure 9a shows the edges with zigzag (top) and armchair (bottom) atomic structure, separated from each other by  $150^\circ$  in real space. The wavevectors of the defects associated with these edges are represented by  $\mathbf{d}_a$  for the armchair edge and  $\mathbf{d}_z$  for the zigzag edge. Figure 9b shows the first Brillouin zone of two-dimensional graphite oriented according to the lattice in real space shown in figure 9a. Note that, for inter-valley scattering, only the armchair  $\mathbf{d}_a$  vector is able to connect points belonging to circles centred at two inequivalent K and K' points. Considering usual laser energies (less than 3 eV), the radii of the circles around the K' and K points are not large enough to allow the connection of any  $\mathbf{k}'$  and  $\mathbf{k}$  states by a zigzag  $\mathbf{d}_z$  vector. Therefore, the inter-valley double-resonance

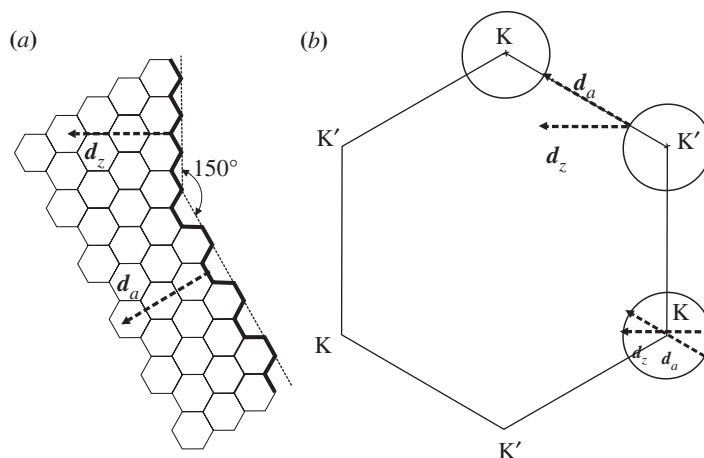


Figure 9. (a) Schematic of the atomic structure of edges in  $r$  space with the zigzag and armchair orientations. The boundaries can scatter electrons with momentum transfer along  $d_z$  for the zigzag edge, and  $d_a$  for the armchair edge. (b) First Brillouin zone of the two-dimensional graphite (graphene), showing defect-induced inter-valley and intra-valley scattering processes. Since  $d_z$  cannot connect the K and K' points, the defect-induced double-resonance inter-valley process is forbidden at zigzag edges (Cançado *et al.* 2004).

process associated with this defect cannot occur for a perfect zigzag edge. The mechanism depicted in figure 9b thus shows that the  $D$ -band scattering process is forbidden in a zigzag edge (Cançado *et al.* 2004).

On the other hand, the  $D'$  band, around  $1620\text{ cm}^{-1}$ , is given by an intra-valley process, which connects points belonging to the same circle around the K (or K') point (see K point in figure 9b). Therefore, the intra-valley process for the  $D'$  band can be satisfied by both  $d_a$  and  $d_z$  vectors and, for this reason, the observation of the  $D'$  band should be largely independent of the edge structure.

Finally, when measuring an armchair edge by Raman spectroscopy, the  $D$ -band intensity will depend strongly on the light polarization direction with respect to the edge direction. The  $D$ -band intensity will be a maximum when the light is polarized along the edge, and zero when the light polarization is crossed with respect to the edge direction. This result is related to the theoretical calculations that predict an anisotropy in the optical absorption (emission) coefficient of two-dimensional graphite, given by (Grüneis *et al.* 2003)

$$W_{\text{abs,ems}} \propto |\mathbf{P} \times \mathbf{k}|^2, \quad (4.1)$$

where  $\mathbf{P}$  is the polarization of the incident (scattered) light for the absorption (emission) process and  $\mathbf{k}$  is the wavevector of the electron measured from the K point. The  $D$ -band intensity is then dependent on the light polarization direction relative to the edge direction.

Recently, Sasaki *et al.* (2010) showed that the phonon softening effect of the  $G$  can characterize the graphene edge structure. In the presence of free electrons, the  $G$  band and the radial breathing mode (RBM) phonon in single-walled carbon nanotubes (SWNTs) becomes soft as a function of the Fermi energy position,



through an effect which is known as the Kohn anomaly (Sasaki *et al.* 2008*a,b*; Farhat *et al.* 2009; Kalbac *et al.* 2009; Park *et al.* 2009). These phenomena occur preferentially at graphene edges, since the electron wave function forms a standing wave by mixing elastically scattered waves at the edge where the momentum along the edge (perpendicular to the edge) is conserved (changes its sign). Here, we select the  $x$  and  $y$  axes for zigzag and armchair edges, respectively, the directions in a rectangular-shaped graphene sample of which can be selected to be perpendicular to each other. Then the scattering event results in a sign change in  $k_y$  and  $k_x$  for zigzag and armchair edges, respectively. At the edges, the electron wave function forms a standing wave which consists of the initial and scattered  $\mathbf{k}$  states. Then the electron–phonon matrix elements at a graphene edge for the  $G$ -band phonon can be calculated by using the standing wave eigenfunction for each of the LO and TO phonon modes for which the vibration direction of the LO and TO phonon modes are parallel and perpendicular to the edge direction. The details of the calculation (Sasaki *et al.* 2010) show that only the LO (TO) phonon mode is Raman active for armchair (zigzag) edges, thereby showing a polarization dependence of the light. On the other hand, only LO phonon modes show a Kohn anomaly effect for both types of edges. Thus, we can distinguish between LO and TO phonon modes by the phonon softening phenomena, and in this way we can use Raman spectroscopy to characterize the edge-structure type. These phenomena should appear for a restricted spatial region near the edge where the concept of the standing wave is well established. The theoretical prediction has already been observed partially by experiment (Sasaki *et al.* 2009). However, more precise experimental observations are still needed as a function of gate voltage or by the polarization direction of the light at a well-defined edge structure, and such work remains for future investigation.

## 5. Specificities of the disorder in the Raman spectra of carbon nanotubes

When moving to carbon nanotubes, the quantum confinement of the electronic structure will constrain the double-resonance processes in SWNTs, similarly to what has been discussed in §4 for graphene.

### (a) The $D$ band in SWNT bundles

A multi-peak structure (Zolyomi *et al.* 2003) and an oscillatory dispersive behaviour (Brown *et al.* 2001) has been observed for the  $D$  band in SWNT bundles. For isolated tubes, unusually sharp features can be seen in the  $D$  band with a full width half maximum (FWHM) intensity linewidth down to  $7\text{ cm}^{-1}$  (Jorio *et al.* 2002) owing to quantum confinement effects. Furthermore, the  $D$ -band frequency also depends on the nanotube diameter, with the following result for 514 nm (2.41 eV) laser excitation (Souza Filho *et al.* 2003):

$$\omega_D = 1354.8 - \frac{16.5}{d_t}. \quad (5.1)$$

Furthermore, the  $D$  band is a second-order process with a phonon frequency  $\omega_D$  related to that of the second order  $G'$  band by  $2\omega_D \simeq \omega_{G'}$ .

Some efforts have been made to quantify disorder in SWNTs, by studying irradiated SWNT samples (Hulman *et al.* 2005), and in SWNTs cut to different lengths (Chou *et al.* 2007). Clear enhancement of the  $D$  band is observed with increasing defect density or with decreasing nanotube lengths. However, because of the lack of direct real-space characterization, the results are not as quantitative as the results obtained in graphene (Lucchese *et al.* 2010) and in nanographite (Cançado *et al.* 2008) and in irradiated double-walled carbon nanotubes (DWNTs), as discussed in §5*b*. Some aspects are still unclear such as why the  $D$  band in metallic SWNTs is usually more intense than in semiconducting tubes. Although some theoretical efforts based on the double-resonance process were directed to address this problem (Maultzsch *et al.* 2001), the predictions (Maultzsch *et al.* 2002, 2003) regarding the  $D$  band are still very incomplete.

(*b*)  $Si^{+}$  and  $C^{+}$  bombarded DWNTs

Resonance Raman scattering spectroscopy has been used to monitor the implantation of Si and C ions into highly purified DWNTs (Saraiva *et al.* 2009). The data indicate that the outer tubes of the DWNTs are more affected by the ion bombardment than the inner tubes. As the ion beam fluence increases, the tubes get disordered, as indicated by the increase in the  $D$  to  $G$  band intensity ratio ( $I_D/I_G$ ), and this effect is much stronger for implantation with Si than with C. In figure 10*a*, we show the plot of  $I_D/I_G$  as a function of the C and Si ion bombardment dose for two different  $E_{\text{laser}}$  values. We can see that the  $I_D/I_G$  ratio increases as the dose increases, thus confirming the increasing density of defects in the DWNT samples with increasing ion fluence. It is also clear that the  $I_D/I_G$  ratio depends strongly on the ion species used for the bombardment, as well as on the  $E_{\text{laser}}$  used for characterization (Saraiva *et al.* 2009).

In order to separate the contributions from the dose and the ion species at each laser excitation energy, we normalized the  $I_D/I_G$  curves from figure 10*a* by  $E_{\text{laser}}^4$  in accordance with the model of Cançado *et al.* (figure 10*b*). Although the model was developed for graphite, this model should apply to some extent to other  $sp^2$ -based materials such as carbon nanotubes. After carrying out this normalization, we can see that the curves for a given ion-implanted sample show a unique curve only for ion doses up to  $2 \times 10^{14}$  ions  $\text{cm}^{-2}$ . Therefore, we can use Cançado's empirical equation for estimating the characteristic length  $L_a$  in this range of ion dose for the bombarded DWNTs. Here, the  $L_a$  should be interpreted as a characteristic distance between the defects on the carbon nanotube lattice introduced by the ion beam. The  $L_a$  values are shown in figure 10*c*. Here, we can see that this characteristic length dependence on ion fluence is stronger for Si bombardment than for C ion bombardment at the same fluence, but both datasets show a tendency towards saturation. It has been demonstrated in the literature that carbon nanotubes when irradiated with electrons exhibit pronounced healing effects. It is possible that the same healing mechanism is operative in the case of ion bombardment, with the healing effect being more efficient in the case of the less damaging carbon irradiation (when compared with silicon irradiation).

The minimum crystallite size used by Cançado *et al.* for obtaining the empirical equation (equation 5.1) was 20 nm. For these ion-bombarded samples, the lowest characteristic length determined from the range of  $L_a$  where the  $I_D/I_G$  ratio follows the  $E_{\text{laser}}^4$  dependence also was about 20 nm (see figure 10*b*). For doses

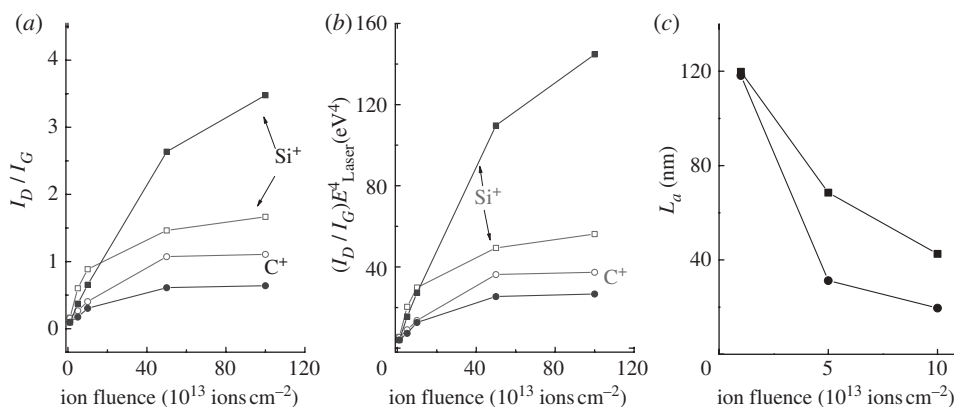


Figure 10. Plots of the dependence on ion fluence of the  $I_D/I_G$  ratio (a) and of the normalized  $(I_D/I_G)E_{\text{laser}}^4$  function versus ion fluence probed by two laser energies (open circle,  $E_{\text{laser}} = 2.41$  eV; filled circle,  $E_{\text{laser}} = 2.54$  eV) and (b) for Si and C ion bombardments. In (c) we plot the characteristic length  $L_a$  for Si (filled circle) and C (filled square) implanted DWNT samples as obtained from the  $I_D/I_G$  intensity ratio using the model of Cançado *et al.* (2008) and Saraiva *et al.* (2009).

larger than  $40 \times 10^{13}$  ions  $\text{cm}^{-2}$ , the experimental data do not exhibit the  $E_{\text{laser}}^4$  dependence any more, and this is attributed to the very large density of defects which translates into a very small crystallite size  $L_a$ . In this limit, the carbon lattice is likely to lose its  $sp^2$ -like character, thus forming amorphous carbon and carbon clusters with a substantial amount of  $sp^3$  bonding. It seems that, for Si-bombarded samples, the fraction of amorphous carbon and  $sp^3$ -like carbon is higher than that of C-bombarded samples. This argument is based on the observation that the Raman cross section for  $sp^3$  carbon is much lower than that for  $sp^2$  carbon. Amorphous carbon nanowires were obtained in multiwalled carbon nanotubes (MWNTs) by high doses ( $10^{15}$ – $10^{17}$  ions  $\text{cm}^{-2}$ ) of a 40 keV Si ion beam. An amorphous carbon nanowire is completely formed for fluences of  $10^{17}$  ions  $\text{cm}^{-2}$ . The lower fluence  $10^{15}$  ions  $\text{cm}^{-2}$  only make the MWNT layers very disordered, which indicates a higher stability against damage by the ion beam than in DWNTs, owing to the considerably larger number of layers in MWNTs.

Finally, the behaviour of the  $I_D/I_G$  ratio as a function of ion fluence rules out the possibility of bombardment-induced nanographite because in the  $10^{15}$  ions  $\text{cm}^{-2}$  regime it is expected that the  $I_D/I_G$  ratio would exhibit an  $L_a^2$  dependence following the Tuinstra model (Tuinstra & Koenig 1970a). This dependence would imply a monotonic decrease in intensity of the curves shown in figure 7, instead of the observed saturation behaviour, thus indicating that the bombardment of C ions is not leading to the formation of nanocrystalline graphite.

## 6. Local effects revealed by near-field measurements

Besides disturbing the momentum conservation of the ordered system, the presence of disorder is expected to change the local electron and phonon structure. The  $G'$ -band feature is not a disorder-induced feature but it can nevertheless be used to probe changes in the electronic and vibrational structure

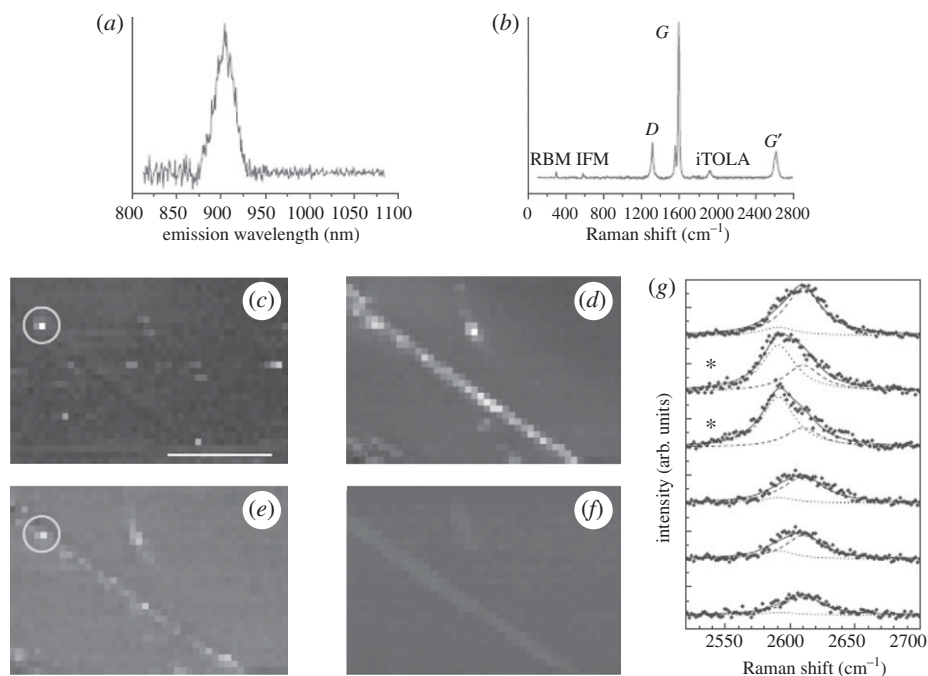


Figure 11. Localized excitonic emission from a semiconducting SWNT. (a) Photoluminescence emission at  $\lambda_{\text{em}} = 900$  nm. (b) A Raman spectrum recorded from the same SWNT as in (a). The spectral peak frequency of the RBM,  $\omega_{\text{RBM}} = 302 \text{ cm}^{-1}$ , together with the  $\lambda_{\text{em}} = 900$  nm information, leads to the (9,1) assignment for this tube. (c) Near-field photoluminescence image of the same SWNT revealing localized excitonic emission. (d,e) Near-field Raman imaging of the same SWNT, where the image contrast is provided by spectral integration over the *G* and *D* bands, respectively. (f) Corresponding topography image for the same SWNT. The circles in (c,e) indicate locations where localized photoluminescence measurements on a specific defect in a carbon nanotube were made in (c) and the defect-induced (*D* band) Raman scattering is shown in (e). The scale bar in (c) denotes 250 nm. (g) Evolution of the *G'*-band spectra near the defective segment of the (9,1) SWNT. The spectra were taken in steps of 25 nm along the nanotube, showing the defect-induced *G'* peak (dotted Lorentzian component lineshapes). The asterisks in (g) denote the spatial locations where localized photoluminescence and defect-induced *D*-band Raman scattering were measured (see circles in (c,e), respectively; Maciel *et al.* 2008b).

related to disorder. The two-dimensional versus three-dimensional stacking order of graphene layers is one example where the *G'* band provides important information. Highly crystalline three-dimensional graphite shows two *G'* peaks (see figure 11g). When the interlayer stacking order is lost, a one-peak feature, identified with two-dimensional graphite, starts to develop, and this peak is centred near the middle of the two peaks in the *G'* lineshape from ordered graphite (see figure 11g). More interesting, localized emission of a red-shifted *G'* band was observed and this emission is related to the local distortion of the nanotube lattice by a negatively charged defect. The defect position was initially located by studying local variations in the *D*-band intensity as described below (Maciel *et al.* 2008b).

Figure 11 shows near-field Raman and near-field photoluminescence spectra and spatial maps for an individual SWNT. The near-field technique can generate spectral information with spatial resolution  $\Delta x$  below the diffraction limit ( $\Delta x \sim \lambda_{\text{laser}}/2$ ) (Novotny & Hecht 2006). In particular, figure 11*a,b* shows the photoluminescence and Raman spectra of defects in a SWNT, respectively, with  $\Delta x \sim 30$  nm. The near-field microscopy measurements from the same SWNT are shown in figure 11*c–f*. In particular, figure 11*c* represents the near-field photoluminescence image of this SWNT, where the image contrast is provided by spectral integration over the photoluminescence peak centred at  $\lambda_{\text{em}} = 900$  nm (see figure 11*a*). The most striking feature in this image is the high degree of spatial localization of the photoluminescence emission along the SWNT. This is evident by inspection of the extended topography image of the nanotube shown in figure 11*f*, and also of the near-field Raman image of the *G* band, with a peak intensity near  $1590\text{ cm}^{-1}$  shown in figure 11*d*. While we observe from figure 11*d* that the *G*-band Raman scattering is present along the entire length of the nanotube, from figure 11*e* we observe an increased defect-induced *D* band at  $1300\text{ cm}^{-1}$  with Raman scattering intensity localized in the *same* spatial region where exciton emission was detected. Defects are known to act as trapping states for electron–hole recombination (i.e. exciton emission), thereby providing insights into the correlations observed between figure 11*a,c*.

Interestingly, when measuring the Raman spectra across the defective spot, sudden changes in many Raman features are observed. It has further been shown by Maciel *et al.* (2008*b*) that substitutional doping in SWNTs causes changes in the *G'*-band spectra owing to charge-induced renormalization of the electronic and vibrational energies. Figure 11*g* shows the *G'* band measured on the same SWNT, moving along the position where the local *D* band and photoluminescence emission is observed (circle in figure 11*e*). The two spectra marked by ‘\*’ in figure 11*g* were obtained at this defect location, and a new peak is observed in the *G'* band region. The frequency and intensity of this new peak depend on the type and level of doping, respectively (Maciel *et al.* 2008*a*, 2009*a,b*). This makes the Raman *G'* band a sensitive probe for studying and quantifying doping, which is a more accurate probe than the *D* band, since the *D* band can also be related to amorphous carbon and any other defective *sp*<sup>2</sup> structure. Also the *D*-band frequency is not so sensitive to the type of defect or dopant. The one-dimensional edge defect selects the direction of the electron and phonon wavevectors associated with the disorder-induced Raman process, and causes a dependence of the Raman *D*-band intensity on the atomic structure of the edge (strong for an armchair edge and weak for a zigzag edge).

The first experimental evidence for the selection rules discussed here was developed for a graphite boundary (Cançado *et al.* 2004). However, similar results have already been shown for monolayer graphene (Casiraghi *et al.* 2009; Gupta *et al.* 2009). Interestingly, up to now variations in the *D*-band intensity have been observed, but never has a complete absence of the *D* band together with the presence of the *D'* band been seen experimentally. This result indicates that, up to now, no perfect zigzag edge structure has been measured by Raman spectroscopy. It should be emphasized that Raman spectroscopy provides one easy method for distinguishing between armchair and zigzag edges. Of course, high-resolution TEM provides another experimental method for distinguishing armchair from zigzag edges (Jia *et al.* 2009).

## 7. Summary

This review focuses on two types of defects in  $sp^2$  carbon nanostructures, namely point defects and edges. Point defects are explicitly studied by controlled argon ion implantation studies of graphene as a function of fluence. Near-field studies at the individual nanotube level using both Raman scattering and photoluminescence probes are used to give high spatial resolution to defect studies. A simple model is given to account for the major findings of these ion implantation studies of point defects. Boundaries and sample edges are shown to behave similarly to defects insofar as they disturb the crystal symmetry and lead to the observation of symmetry-breaking spectral features, such as the  $D$  band and the  $D'$  band in the Raman spectra. Differences in the selection rules for zigzag and armchair edges lead to the important result that armchair edges show strong  $D$ -band intensity while zigzag edges do not, thereby providing a sensitive tool for distinguishing between armchair and zigzag edges spectroscopically.

A.J. acknowledges support from CNPq, Brazil, and AFOSR/SOARD (award no. FA9550-08-1-0236). M.S.D. acknowledges support from NSF-DMR 07-04197 and the ONR GATE MURI project monitored by Dr Chagaan Baatar under N00014-09-1-1063. R.S. acknowledges support from MEXT grant (no. 20241023). A.G.S.F. acknowledges support from CNPq grants no. 306335/2007-7, no. 503956/2007-4, and no. 577489/2008-9, Rede Nacional de Pesquisa em Nanotubos de Carbono, European Union Seventh Framework Programme (FP7) Small Collaborative project, Neuronano (NMP4-SL-2008-214547), and INCT NanoBioSimes.

## References

- Ashcroft, N. W. & Mermin, N. D. 1976 *Solid state physics*. New York, NY: Holt, Rinehart and Winston, p. 141.
- Baranov, A. V., Bekhterev, A. N., Bobovich, Y. S. & Petrov, V. I. 1987 Interpretation of some features in the Raman spectrum of graphite and glassy carbon. *Opt. Spectrosc.* **62**, 1036.
- Barros, E. B., Demir, N. S., Souza Filho, A. G., Mendes Filho, J., Jorio, A. J., Dresselhaus, G. & Dresselhaus, M. S. 2005 Raman spectroscopy of graphitic foams. *Phys. Rev. B* **71**, 165422. (doi:10.1103/PhysRevB.71.165422)
- Basko, D. M. B. 2008 Theory of resonant multiphonon Raman scattering in graphene. *Phys. Rev. B* **78**, 125418. (doi:10.1103/PhysRevB.78.125418)
- Brown, S. D. M., Jorio, A., Dresselhaus, M. S. & Dresselhaus, G. 2001 Observation of the  $D$ -band feature in the Raman spectra of carbon nanotubes. *Phys. Rev. B* **64**, 073403. (doi:10.1103/PhysRevB.64.073403)
- Cançado, L. G., Pimenta, M. A., Neves, B. R., Dantas, M. S. & Jorio, A. 2004 Influence of the atomic structure on the Raman spectra of graphite edges. *Phys. Rev. Lett.* **93**, 247401. (doi:10.1103/PhysRevLett.93.247401)
- Cançado, L. G., Jorio, A. & Pimenta, M. A. 2007 Measuring the absolute Raman cross section of nanographites as a function of laser energy and crystallite size. *Phys. Rev. B* **76**, 064304. (doi:10.1103/PhysRevB.76.064304)
- Cançado, L. G., Takai, K., Enoki, T., Endo, M., Kim, Y. A., Mizusaki, H., Speziali, N. L., Jorio, A. & Pimenta, M. A. 2008 Measuring the degree of stacking order in graphite by Raman spectroscopy. *Carbon* **46**, 272–275. (doi:10.1016/j.carbon.2007.11.015)
- Cardona, M. 1982 Resonance phenomena. In *Light-scattering in solids, topics in applied physics*, vol. 50 (eds M. Cardona & G. Güntherodt), p. 19. Berlin, Germany: Springer.
- Casiraghi, C., Hartschuh, A., Qian, H., Piscanec, S., Georgi, C., Fasoli, A., Novoselov, K. S., Basko, D. M., & Ferrari, A. C. 2009 Raman spectroscopy of graphene edges. *Nano Lett.* **9**, 1433–1441. (doi:10.1021/nl8032697)



- Chou, S. G., Son, H., Kong, J., Jorio, A., Saito, R., Zheng, M., Dresselhaus, G. & Dresselhaus, M. S. 2007 Length characterization of DNA-wrapped carbon nanotubes using Raman spectroscopy. *Appl. Phys. Lett.* **90**, 131109. (doi:10.1063/1.2713121)
- Dresselhaus, M. S. & Kalish, R. 1992 *Ion implantation in diamond, graphite and related materials*. Springer Series in Materials Science, no. 22. Berlin, Germany: Springer.
- Dresselhaus, M. S., Dresselhaus, G., Saito, R. & Jorio, A. 2005 Raman spectroscopy of carbon nanotubes. *Phys. Rep.* **409**, 47–99. (doi:10.1016/j.physrep.2004.10.006)
- Farhat, H., Sasaki, K., Kalbac, M., Hofmann, M., Saito, R., Dresselhaus, M. S. & Kong, J. 2009 Softening of the radial breathing mode in metallic carbon nanotubes. *Phys. Rev. Lett.* **102**, 126804. (doi:10.1103/PhysRevLett.102.126804)
- Ferrari, A. C. & Robertson, J. 2000 Interpretation of Raman spectra of disordered and amorphous carbon. *Phys. Rev. B* **61**, 14095. (doi:10.1103/PhysRevB.61.14095)
- Ferrari, A. C. & Robertson, J. (eds) 2004 Raman spectroscopy in carbons: from nanotubes to diamond. *Phil. Trans. R. Soc. A* **362**, 2269–2565. (doi:10.1098/rsta.2004.1453)
- Ferreira, E. H. M., Moutinho, M. V. O., Stavale, F., Lucchese, M. M., Capaz, R. B., Achete, C. A. & Jorio, A. In press. Evolution of the Raman spectra from single, few and many layers graphene with increasing disorder. *Phys. Rev. B Condens. Matter*.
- Grüneis, A. *et al.* 2003 Inhomogeneous optical absorption around the K point in graphite and carbon nanotubes. *Phys. Rev. B* **67**, 165402. (doi:10.1103/PhysRevB.67.165402)
- Gupta, A. K., Russin, T. J., Gutierrez, H. R. & Eklund, P. C. 2009 Probing graphene edges via Raman scattering. *ACS Nano* **3**, 45–52. (doi:10.1021/nm8003636)
- Hulman, M., Skakalova, V., Roth, S. & Kuzmany, H. 2005 Raman spectroscopy of single-wall carbon nanotubes and graphite irradiated by  $\gamma$  rays. *J. Appl. Phys.* **98**, 024311. (doi:10.1063/1.1984080)
- Jia, X. *et al.* 2009 Controlled formation of sharp zigzag and armchair edges in graphene nanoribbons. *Science* **323**, 1701–1705. (doi:10.1126/science.1166862)
- Jorio, A. *et al.* 2002 Linewidth of the Raman features of individual single-wall carbon nanotubes. *Phys. Rev. B* **66**, 115411. (doi:10.1103/PhysRevB.66.115411)
- Jorio, A., Dresselhaus, M. S. & Dresselhaus, G. 2008 *Carbon nanotubes: advanced topics in the synthesis, structure, properties and applications*. Springer Series on Topics in Applied Physics, no. 111. Berlin, Germany: Springer.
- Jorio, A., Lucchese, M. M., Stavale, F. & Achete, C. A. 2009 Raman spectroscopy study of Ar bombardment in highly oriented pyrolytic graphite. *Phys. Status Solidi (b)* **246**, 2689–2692. (doi:10.1002/pssb.200982314)
- Jorio, A., Lucchese, M. M., Stavale, F., Martins Ferreira, E. H., Moutinho, M. V. O., Capaz, R. B. & Achete, C. 2010a Raman study of ion-induced defects in *N*-layer graphene. *J. Phys. Condens. Matter* **22**, 334204. (doi:10.1088/0953-8984/22/33/334204)
- Jorio, A., Saito, R., Dresselhaus, G. & Dresselhaus, M. S. 2010b *Raman spectroscopy in graphene related systems*. Weinheim, Germany: Wiley-VCH Verlag GmbH & Co KGaA.
- Jorio, A., Ferreira, E. H. M., Moutinho, M. V. O., Stavale, F., Achete, C. A. & Capaz, R. B. In press. Measuring disorder in graphene with the G and D bands. *Phys. Status Solidi (b)*.
- Kalbac, M., Farhat, H., Kavan, L., Kong, J., Sasaki, K., Saito, R. & Dresselhaus, M. S. 2009 Electrochemical charging of individual single-walled carbon nanotubes. *Nano (ACS)* **3**, 2320.
- Kittel, C. 1986 *Introduction to solid state physics*, 6th edn. New York, NY: Wiley.
- Knight, D. S. & White, W. B. 1989 Characterization of diamond films by Raman spectroscopy. *J. Mater. Res.* **4**, 385–393. (doi:10.1557/JMR.1989.0385)
- Lazzeri, M., Attaccalite, C. & Mauri, F. 2008 Impact of the electron-electron correlation on phonon dispersion: failure of LDA and GGA DFT functionals in graphene and graphite. *Phys. Rev. B* **78**, 081406(R). (doi:10.1103/PhysRevB.78.081406)
- Lespade, P., Al-Jishi, R. & Dresselhaus, M. S. 1982 Model for Raman scattering from incompletely graphitized carbons. *Carbon* **20**, 427–431. (doi:10.1016/0008-6223(82)90043-4)
- Lespade, P., Marchand, A., Couzi, M. & Cruge, F. 1984 Caractérisation de matériaux carbonés par microspectrométrie Raman. *Carbon* **22**, 375–385. (doi:10.1016/0008-6223(84)90009-5)
- Lucchese, M. M., Stavale, F., Martins Ferreira, E. H., Vilane, C., Moutinho, M. V. O., Capaz, R. B., Achete, C. A. & Jorio, A. 2010 Quantifying ion-induced defects and Raman relaxation length in graphene. *Carbon* **28**, 1592–1597. (doi:10.1016/j.carbon.2009.12.057)

- Maciel, I. O., Pimenta, M. A., Terrones, M., Terrones, H., Campos-Delgado, J. & Jorio, A. 2008a The two peaks  $G'$  band in carbon nanotubes. *Phys. Status Solidi (b)* **254**, 2197–2200. (doi:10.1002/pssb.200879623)
- Maciel, I. O. et al. 2008b Electron and phonon renormalization near charged defects in carbon nanotubes. *Nat. Mater.* **7**, 878. (doi:10.1038/nmat2296)
- Maciel, I. O. et al. 2009a Synthesis, electronic structure, and raman scattering of phosphorus-doped single-wall carbon nanotubes. *Nano Lett.* **9**, 2267–2272. (doi:10.1021/nl9004207)
- Maciel, I. O., Campos-Delgado, J., Pimenta, M. A., Terrones, M., Terrones, H., Rao, A. M. & Jorio, A. 2009b Boron, nitrogen and phosphorous substitutionally doped single-wall carbon nanotubes studied by resonance Raman spectroscopy. *Phys. Status Solidi (b)* **246**, 2432–2435. (doi:10.1002/pssb.200982254)
- Martin, R. M. & Falicov, L. M. 1975 Resonant Raman scattering. In *Light-scattering in solids, topics in applied physics*, vol. 8 (ed. M. Cardona), p. 80. Berlin, Germany: Springer.
- Maultzsch, J., Reich, S. & Thomsen, C. 2001 Chirality-selective Raman scattering of the D mode in carbon nanotubes. *Phys. Rev. B* **64**, 121407(R). (doi:10.1103/PhysRevB.64.121407)
- Maultzsch, J., Reich, S. & Thomsen, C. 2002 Raman scattering in carbon nanotubes revisited. *Phys. Rev. B* **65**, 233402. (doi:10.1103/PhysRevB.65.233402)
- Maultzsch, J., Reich, S., Schlecht, U. & Thomsen, C. 2003 High-energy phonon branches of an individual metallic carbon nanotube. *Phys. Rev. Lett.* **91**, 087402. (doi:10.1103/PhysRevLett.91.087402)
- Mernagh, T. P., Cooney, R. P. & Johnson, R. A. 1984 Raman spectra of Graphon carbon black. *Carbon* **22**, 39–42. (doi:10.1016/0008-6223(84)90130-1)
- Meyer, J. C., Paillet, M., Michel, T., Moréac, A., Neumann, A., Duesberg, G. S., Roth, S. & Sauvajol, J. L. 2005 Raman modes of index-identified freestanding single-walled carbon nanotubes. *Phys. Rev. Lett.* **95**, 217401. (doi:10.1103/PhysRevLett.95.217401)
- Nemanich, R. J. & Solin, S. A. 1977 Observation of an anomalously sharp feature in the 2nd order Raman spectrum of graphite. *Solid State Commun.* **23**, 417–420. (doi:10.1016/0038-1098(77)90998-X)
- Nemanich, R. J. & Solin, S. A. 1979 First- and second-order Raman scattering from finite-size crystals of graphite. *Phys. Rev. B* **20**, 392–401. (doi:10.1103/PhysRevB.20.392)
- Novoselov, K. S., Geim, A. K., Morozov, S. V., Jiang, D., Katsnelson, M. I., Grigorieva, I. V., Dubonos, S. V. & Firsov, A. A. 2005 Two-dimensional gas of massless Dirac fermions in graphene. *Nature* **438**, 197–200. (doi:10.1038/nature04233)
- Novotny, L. & Hecht, B. 2006 *Principles of nano-optics*. Cambridge, UK: Cambridge University Press.
- Park, J. S., Sasaki, K., Saito, R., Izumida, W., Kalbac, M., Farhat, H., Dresselhaus, G. & Dresselhaus, M. S. 2009 Fermi energy dependence of the  $G$  band resonance Raman spectra of single walled carbon nanotubes. *Phys. Rev. B* **80**, 081402. (doi:10.1103/PhysRevB.80.081402)
- Pimenta, M. A., Dresselhaus, G., Dresselhaus, M. S., Cançado, L. G., Jorio, A. & Saito, R. 2007 Studying disorder in graphite-based systems by Raman spectroscopy. *Phys. Chem. Chem. Phys.* **9**, 1276–1290. (doi:10.1039/b613962k)
- Saito, R., Jorio, A., Souza Filho, A. G., Dresselhaus, G., Dresselhaus, M. S. & Pimenta, M. A. 2002 Probing phonon dispersion relations of graphite by double resonance Raman scattering. *Phys. Rev. Lett.* **88**, 027401. (doi:10.1103/PhysRevLett.88.027401)
- Saraiva, G. D. et al. 2009 Resonant raman spectroscopy in Si and C ion-implanted double wall carbon nanotubes. *Phys. Rev. B* **80**, 155452. (doi:10.1103/PhysRevB.80.155452)
- Sasaki, K., Saito, R., Dresselhaus, G., Dresselhaus, M. S., Farhat, H. & Kong, J. 2008a Chirality dependent frequency shift of radial breathing mode in metallic carbon nanotubes. *Phys. Rev. B* **78**, 235405. (doi:10.1103/PhysRevB.78.235405)
- Sasaki, K., Saito, R., Dresselhaus, G., Dresselhaus, M. S., Farhat, H. & Kong, J. 2008b Curvature-induced optical phonon frequency shift in metallic carbon nanotubes. *Phys. Rev. B* **77**, 245441. (doi:10.1103/PhysRevB.77.245441)
- Sasaki, K., Yamamoto, M., Wakabayashi, K., Mori, T., Takai, K., Enoki, T., Saito, R. & Dresselhaus, M. S. 2009 Kohn anomalies in graphene nanoribbons. *Phys. Rev. B* **80**, 155450. (doi:10.1103/PhysRevB.80.155450)

- Sasaki, K., Saito, R., Wakabayashi, K. & Enoki, T. 2010 Identifying the orientation of edge of graphene using G band Raman spectra. *J. Phys. Soc. Jpn.* **79**, 044603. (doi:10.1143/JPSJ.79.044603)
- Sato, K. *et al.* 2006 D-band Raman intensity of graphitic materials as a function of laser energy and crystallite size. *Chem. Phys. Lett.* **427**, 117–121. (doi:10.1016/j.cplett.2006.05.107)
- Souza Filho, A. G. *et al.* 2003 Competing spring constant versus double resonance effects on the properties of dispersive modes in isolated single wall carbon nanotubes. *Phys. Rev. B* **67**, 035427. (doi:10.1103/PhysRevB.67.035427)
- Thomsen, C. & Reich, S. 2000 Double resonant Raman scattering in graphite. *Phys. Rev. Lett.* **85**, 5214–5217. (doi:10.1103/PhysRevLett.85.5214)
- Tsu, R., Gonzalez, J. H. & Hernandez, I. C. 1978 Observation of splitting of the  $E_{2g}$  mode and two-phonon spectrum in graphites. *Solid State Commun.* **27**, 507–510. (doi:10.1016/0038-1098(78)90382-4)
- Tuinstra, F. & Koenig, J. L. 1970a Raman spectrum of graphite. *J. Chem. Phys.* **53**, 1126. (doi:10.1063/1.1674108)
- Tuinstra, F. & Koenig, J. L. 1970b Raman scattering of graphite. *J. Comp. Mater.* **4**, 492.
- Vidano, R. P., Fishbach, D. B., Willis, L. J. & Loehr, T. M. 1981 Observation of raman band shifting with excitation wavelength for carbons and graphites. *Solid State Commun.* **39**, 341–344. (doi:10.1016/0038-1098(81)90686-4)
- Wilhelm, H., Lelausian, M., McRae, E. & Humbert, B. 1998 Raman spectroscopic studies on well-defined carbonaceous materials of strong two-dimensional character. *J. Appl. Phys.* **84**, 6552. (doi:10.1063/1.369027)
- Zhang, Y. B., Tan, Y. W., Stormer, H. L. & Kim, P. 2005 Experimental observation of the quantum Hall effect and Berry's phase in graphene. *Nature* **438**, 201–204. (doi:10.1038/nature04235)
- Zolyomi, V., Kurti, J., Grüneis, A. & Kuzmany, H. 2003 Origin of the fine structure of the Raman *D* band in single-wall carbon nanotubes. *Phys. Rev. Lett.* **90**, 157401. (doi:10.1103/PhysRevLett.90.157401)